Temperature-Insensitive Irreversible Demagnetization Fault Diagnosis Based on Dual-State Flux Estimation for PMSMs

Jinqiu Gao, Weihua Gui, *Member, IEEE*, Xiaotian Xie, *Member, IEEE*, Rongchun Wan, Shicai Yin, and Chunhua Yang, *Fellow, IEEE*

***Abstract*—This article proposes a temperature-insensitive irreversible demagnetization (ID) fault diagnosis based on dual-state flux estimation for permanent magnet synchronous motors considering temperature influence. The methodology employs dual-state extended state observers (ESOs) to accurately capture system disturbances and compute the real magnetic flux through full-rank fourth-order discrete equations, leveraging the particle swarm optimization algorithm. This approach ensures precise flux estimation unaffected by other parameter disturbances. Additionally, a novel temperature estimation strategy utilizing the multiprecision physics-informed neural network (MP-PINN) is proposed, which synthesizes physical knowledge from a lumped parameter thermal network and empirical data, achieving high accuracy and generalization with limited high-precision data. The ID faults are diagnosed by correlating the estimated flux and temperature, with a threshold set considering the temperature's effect on the permanent magnet's remanence characteristics, thus avoiding misdiagnosis of reversible changes as irreversible faults and enhancing diagnostic accuracy. The article systematically elaborates on the dual-state ESO-based flux estimation method, the MP-PINN-based temperature estimation approach, and the comprehensive ID fault diagnosis process, supported by experimental validations that underscore the effectiveness of the proposed solution.**

***Index Terms*—Demagnetization diagnosis, permanent magnet synchronous motor, physics-informed neural network, temperature estimation.**

I. Introduction

PERMANENT magnet synchronous motors (PMSMs) have gained increasing attention due to the advantages of high efficiency, high torque density, and low loss, making them a promising candidate for various applications such as high-speed trains and electric vehicles [1], [2]. As the actuator of the traction system, it operates in the environment of narrow space, poor heat dissipation, and continuous vibration for a long time, which makes it a major fault source in rail vehicles [3]. All of these factors can lead to irreversible demagnetization (ID) of the permanent magnets (PMs) resulting in demagnetization faults, which is a fatal problem for the motor system [4]. The ID fault significantly degrade the performance of PMSMs, leading to a decrease in energy efficiency and torque output [5]. Therefore, developing effective and accurate fault diagnosis methods is crucial for rail transit facilities to maintain continuous and reliable operation [6].

Traditional demagnetization fault diagnosis methods for motors are generally classified into three categories: 1) signal processing-based, 2) data-based, and 3) model-based methods [7], [8], [9], [10], [11]. Signal-based fault diagnosis methods leverage the analysis of signals measured by physical sensors. For instance, after analyzing the amplitude and frequency variations of back electromotive forces (EMFs), [10] develops an indirect measurement method to diagnose the demagnetization faults of a PMSM. Data-based fault diagnosis methods focus on learning behavioral patterns and characteristics from system data, and applying these insights for fault diagnosis. Data-based diagnostic methods rely on a large amount of high-quality data and prior knowledge, requiring high standards for real-time data acquisition and processing [12]. Model-based fault diagnosis relies on mathematical models of dynamic systems to obtain prior knowledge, encompassing techniques like state estimation and parameter estimation, all of which depend on the mathematical modeling of the diagnosed object [13]. Meng and Zhang [14] used a sliding-mode flux observer for direct torque control of PMSMs, enhancing flux estimation at very low speeds without needing a speed adaptation mechanism. A developed Kalman filter using current and magnet flux as state variables in the synchronous reference frame was employed to dynamically estimate of rotor permanent magnet (PM) flux [15].

Model-based fault diagnosis methods, particularly those based on flux estimation, offer significant advantages over signal- and data-based methods, such as reduced sensor requirements and enhanced precision and reliability, making them ideal for applications where cost-effectiveness and operational efficiency are crucial. Flux estimation methods typically rely

Received 22 October 2024; revised 27 January 2025 and 31 March 2025; accepted 29 April 2025. Date of publication 8 May 2025; date of current version 30 June 2025. This work was supported in part by the National Natural Science Foundation of China under Grant 62233012, Grant 62173350, and Grant 62403495, in part by the Key Laboratory of Energy Saving Control and Safety Monitoring for Rail Transportation under Grant 2017TP1002. Recommended for publication by Associate Editor A. Trzynadlowski. *(Corresponding author: Xiaotian Xie.)*

Jinqiu Gao is with the School of Water Resources and Hydropower Engineering, Xi'an University of Technology, Xi'an 710048, China (e-mail: gaojinqiu@xaut.edu.cn).

Weihua Gui, Xiaotian Xie, Rongchun Wan, Shicai Yin, and Chunhua Yang are with the School of Automation, Central South University, Changsha 410083, China (e-mail: gwh@csu.edu.cn; xxt_csu@csu.edu.cn; rongchunwan@csu.edu.cn; yinshicai3322@csu.edu.cn; ychh@csu.edu.cn).

Color versions of one or more figures in this article are available at https://doi.org/10.1109/TPEL.2025.3568276.

Digital Object Identifier 10.1109/TPEL.2025.3568276

on flux observers to estimate real-time flux linkage [16]. By comparing the estimated flux linkage with a predefined reference value (corresponding to a healthy motor), these methods can effectively detect demagnetization faults. So far, several flux estimation techniques have been proposed. For instance, Lai et al. [17] introduced a flux linkage estimation method that utilizes a linear Luenberger state observer to determine the EMF, enabling subsequent flux linkage identification. In [18], an adaptive flux estimation approach based on a multiple-model extended Kalman filter with a Markov chain is presented. Meanwhile, Chen et al. [19] proposed a high-robustness sliding mode rotor flux observer capable of detecting real-time air-gap flux linkage. Instead of directly estimating flux linkage, Han et al. [20] employed a sliding mode observer to detect real-time disturbances, which are then used to derive flux information. However, these methods typically overlook the impact of temperature variations on PMSM performance, which is particularly critical in applications such as high-speed trains, where motors are exposed to fluctuating temperatures. These fluctuations can significantly affect motor parameters and the accuracy of model-based flux estimations [21]. Elevated temperatures can lead to reversible demagnetization of PMs, which reduces motor flux but does not constitute an irreversible fault [22], [23]. As the temperature returns to normal, the flux recovers, indicating that the fault is not irreversible [24]. If the motor flux is estimated to be lower than its standard value under these conditions, it could lead to an incorrect fault diagnosis. Therefore, implementing accurate temperature monitoring techniques is crucial to improving the reliability and effectiveness of ID fault diagnosis, particularly in high-speed train applications.

Temperature monitoring methods can be broadly categorized into three types: 1) sensor-based direct measurements, 2) model-based estimations, and 3) data-driven approaches. Although sensor-based temperature measurements can provide fast and precise information about the internal temperature of PMSMs, it is often challenging and not economically feasible actually [25]. Therefore, alternative methods for estimating the internal temperature of PM are needed [26]. In recent years, various temperature estimation methods have been proposed, including analytical models, the electrical parameter identification methods, lumped-parameter thermal network (LPTN) models, and machine learning-based approaches [27]. LPTN models represent the internal heat transfer using thermodynamic theories, but they are highly sensitive to parameter variations and measurement errors, which can significantly affect the accuracy of temperature estimation [28], [29]. Additionally, data-driven methods, which rely on empirical data, are often less interpretable than LPTNs and require large datasets for training, making them less reliable when data quality or quantity is insufficient [30], [31], [32]. These challenges have long been recognized as key obstacles to the effectiveness of machine learning techniques in this domain [33].

This article proposes a temperature-insensitive irreversible demagnetization fault diagnosis based on dual-state flux estimation for PMSMs. The main contributions and novelties of this article can be summarized as follows.

1) A dual-state extended state observer (ESO) is designed to simultaneously estimate both magnetic flux and temperature disturbances. By integrating these two states using full-rank fourth-order discrete equations and the particle swarm optimization (PSO) algorithm, the proposed method enhances flux estimation accuracy, which remains unaffected by external disturbances.
2) A temperature estimation method based on a multi-precision physics-informed neural network (MP-PINN) is introduced. The MP-PINN model is trained with low-precision data derived from a constructed LPTN, achieving high estimation accuracy and generalization performance, even with limited high-precision data.
3) The ID fault diagnosis is improved by integrating flux values from the dual-state ESO with temperature estimated from the MP-PINN. This combined approach dynamically adjusts a critical threshold based on temperature-induced variations in PM material properties, thereby preventing misclassification of reversible thermal effects as ID faults. This methodology significantly improves the accuracy and reliability of fault diagnosis.

The rest of this article is organized as follows. Section II presents the dual-state ESO-based flux estimation method for PMSMs. In Section III, the MP-PINN method is proposed to estimate the real-time PM temperature. In Section IV, considering the influence of temperature and the estimated flux linkage, the ID fault diagnosis of PMSM is carried out. The experimental results of the proposed algorithms are illustrated in Section IV. Section V provide verifications. Finally, Section VI concludes this article.

II. Dual-State ESO-Based Flux Estimation Method for PMSMs

When a demagnetization fault occurs in a PMSM, the actual inductance changes due to variations in the magnetic field, and resistance changes with internal temperature variations. Under these circumstances, traditional observers, which rely on accurate motor models, become less effective because the parameters in the model may change. This leads to an inability to accurately estimate the motor's flux, reducing the accuracy of model-based magnetic flux estimation methods. Therefore, a dual-state ESO-based flux estimation method for PMSMs is proposed.

A. Establishing the ESOs for PMSMs

The model of PMSMs in the dq-axis reference frame, crucial for the intended strategy of demagnetization fault diagnosis, can be characterized by specific differential equations. Considering the small impact of iron saturation and eddy currents, they are overlooked in the mathematical model of the PMSMs, which can be expressed as follows:

$$\begin{cases} \frac{\mathrm{d}i_d}{\mathrm{d}t} = -\frac{R_s}{L_d} i_d + \frac{L_q}{L_d}\omega_e i_q + \frac{u_d}{L_d} \\ \frac{\mathrm{d}i_q}{\mathrm{d}t} = -\frac{L_d}{L_q} p\omega_m i_d - \frac{R_s}{L_q} i_q + \frac{u_q}{L_q} - \frac{\Psi_f}{L_q}\omega_e \end{cases} \tag{1}$$

where i_d, i_q are stator dq-axis currents, u_d, u_q are dq-axis control voltages, L_d, L_q are the real dq-axis inductances, R_s is stator winding resistance, ω_e represents rotor electrical angular speed, and ψ_f is the real rotor flux linkage.

The PMSM model, which includes motor current differential terms, presents a challenge for accurate measurement in practical experiments, making it difficult to precisely estimate the motor parameters in subsequent analyses. Therefore, it is necessary to isolate the current differential terms from the state variables that contain the motor parameters, facilitating the subsequent parameter identification. So, the ultralocal model of the motor can be expressed as:

$$\begin{cases} \frac{di_d}{dt} = \frac{1}{L_d}u_d + f_{de} \\ \frac{di_q}{dt} = \frac{1}{L_q}u_d + f_{qe} \end{cases} \tag{2}$$

$$\begin{cases} f_{de} = -\frac{R_s}{L_d}i_d + \frac{L_q}{L_d}\omega_e i_q \\ f_{qe} = -\frac{L_d}{L_q}\omega_e i_d - \frac{R_s}{L_q}i_q - \frac{\Psi_f}{L_q}\omega_e \end{cases} \tag{3}$$

where f_{de} and f_{qe} are the natural response of the dq-axis current, also known as the total current disturbance.

But when temperature variations occur or demagnetization faults happen in the PMSMs, the electrical parameters of the motor such as inductances often change and no longer align with the specifications listed on the nameplate. Under these circumstances, (2) and (3) can be revised as follows:

$$\begin{cases} \frac{di_d}{dt} = \frac{1}{L_{d\_mea}}u_d + f_{de} \\ \frac{di_q}{dt} = \frac{1}{L_{q\_mea}}u_d + f_{qe} \end{cases} \tag{4}$$

$$\begin{cases} f_{de} = (\frac{1}{L_d} - \frac{1}{L_{d\_mea}})u_d - \frac{R_s}{L_d}i_d + \frac{L_q}{L_d}\omega_e i_q \\ f_{qe} = (\frac{1}{L_q} - \frac{1}{L_{q\_mea}})u_q - \frac{L_d}{L_q}\omega_e i_d - \frac{R_s}{L_q}i_q - \frac{\Psi_f}{L_q}\omega_e \end{cases} \tag{5}$$

where L_{d_mea}, L_{q_mea} are the measured dq-axis inductances.

Disturbances, treated as system state variables, can be estimated with an ESO. A linear ESO, designed based on the aforementioned model, is presented as follows:

$$\begin{cases} e_d = i_d - \widehat{i_d} \\ \frac{d\widehat{i_d}}{dt} = \frac{di_d}{dt} + \beta_1 e_d = \frac{1}{L_{d\_mea}}u_d + \widehat{f_{de}} \\ \frac{d\widehat{f_{de}}}{dt} = \beta_2 e_d \end{cases} \tag{6}$$

$$\begin{cases} e_q = i_q - \widehat{i_q} \\ \frac{d\widehat{i_q}}{dt} = \frac{di_q}{dt} + \beta_1 e_q = \frac{1}{L_{q\_mea}}u_q + \widehat{f_{qe}} \\ \frac{d\widehat{f_{qe}}}{dt} = \beta_2 e_q. \end{cases} \tag{7}$$

From (6) and (7), the transfer function between the error e and the disturbance d can be obtained as follows:

$$G_e(s) = \frac{e(s)}{d(s)} = \frac{s}{s^2 + \beta_1 s + \beta_2}. \tag{8}$$

The relationship between the estimated disturbance $\widehat{f_e}(s)$and the actual disturbance $d(s)$ is obtained through the following transfer function:

$$G_d(s) = \frac{\widehat{f_e}(s)}{d(s)} = \frac{\beta_2}{s}\frac{s}{s^2 + \beta_1 s + \beta_2} = \frac{\beta_2}{s^2 + \beta_1 s + \beta_2}. \tag{9}$$

The observer gains for the ESO are selected based on the following principle to streamline the parameter tuning process, as outlined in [34]:

$$s^2 + \beta_1 s + \beta_2 = (s + \omega_0)^2, \omega_0 > 0. \tag{10}$$

From (10), it is observable that the stability of the ESO is ensured when the roots of the characteristic polynomial are negative.

B. Dual-State Flux Estimation for PMSMs

The dual-state flux estimation method for PMSMs is designed to optimize the accuracy of estimating parameters by employing disturbance equations under different steady-state conditions. This methodological choice addresses a common challenge in motor parameter identification: accurately determining the four key parameters (R_s, L_d, L_q, ψ_f) from typically underdetermined systems. In conventional motor state equations, there are typically only two equations available, but they contain four unknown parameters. This results in an underdetermined system, making it impossible to solve for all parameters directly. By introducing multiple steady-state conditions, the dual-state approach provides additional information, allowing for a more complete and reliable estimation of the motor parameters.

Under steady-state conditions, as seen from (2), the motor's current behavior is influenced by continuous but consistent disturbances. To capture these subtle disturbances and create a robust flux estimation model, we formulate two sets of equations for similar steady states. This dual-state approach diversifies the steady-state conditions, enriching the system of equations. The selection of steady states can be made from various operating points within the motor's typical working domain, ensuring that the system's behavior remains predictable and stable.

When the motor is running in a steady state at t_j, the system can be written as:

$$\begin{cases} f_{de}(t_j) = (\frac{1}{L_d} - \frac{1}{L_{d\_mea}})u_d(t_j) - \frac{R_s}{L_d}i_d(t_j) + \frac{L_q}{L_d}\omega_e i_q(t_j) \\ f_{qe}(t_j) = (\frac{1}{L_q} - \frac{1}{L_{q\_mea}})u_q(t_j) - \frac{L_d}{L_q}\omega_e i_d(t_j) - \frac{R_s}{L_q}i_q(t_j) \\ \qquad\qquad - \frac{\Psi_f}{L_q}\omega_e(t_j). \end{cases} \tag{11}$$

Considering that the actual time intervals between different steady states may not always be predictable, in some cases, this could result in long waiting times, affecting the real-time performance of the algorithm. To address this issue, the proposed method injects a small fixed current into the d-axis. Subsequently, the different state equation at t_h is obtained:

$$\begin{cases} f_{de}(t_h) = (\frac{1}{L_d} - \frac{1}{L_{d\_mea}})u_d(t_h) - \frac{R_s}{L_d}i_d(t_h) + \frac{L_q}{L_d}\omega_e i_q(t_h) \\ f_{qe}(t_h) = (\frac{1}{L_q} - \frac{1}{L_{q\_mea}})u_q(t_h) - \frac{L_d}{L_q}\omega_e i_d(t_h) - \frac{R_s}{L_q}i_q(t_h) \\ \qquad\qquad - \frac{\Psi_f}{L_q}\omega_e(t_h). \end{cases} \tag{12}$$

By implementing two sets of steady-state conditions that subtly vary, a full-rank system of (11) and (12) is created. Given the nonlinear complexity of these equations, it makes it challenging to obtain solutions directly. Unlike solving two equation set, which may result in higher error due to specific sampling times (t_j and t_h, t_{j+1} and t_{h+1}, …, t_{j+i} and t_{h+i}), PSO simultaneously considers multiple sets of equations. The PSO improves flux estimation accuracy by searching for the optimal solution across the full-rank equations under different sampling times. This strategy not only guarantees precise parameter identification but also enhances the model's robustness, enabling it to

adapt effectively to operational variations within typical PMSM settings and improving its resilience.

The PSO algorithm draws inspiration from the observational study of bird flocking and information transfer during foraging. In this algorithm, each individual bird is represented as a "particle," which corresponds to a feasible solution. Z_i denote the position of the ith particle. The fitness of Z_i is calculated using a predefined fitness function, which serves to assess the quality of the particle's position. The velocity of particle i, denoted as V_i, represents the distance moved by the particle in a unit of time. Each particle retains a record of its best position, known as P_i, and the entire swarm collectively maintains a record of the best position found, referred to as P_g. The algorithm iteratively updates the positions and velocities of the particles based on their individual experiences P_i and the collective knowledge P_g, guiding the swarm toward optimal solutions in a problem's search space.

During each iteration of the particles, their update formulas are as follows:

$$\begin{cases} V_i^{k+1} = \omega V_i^k + c_1 r_1 (P_i - Z_i^k) + c_2 r_2 (P_g - Z_i^k) \\ Z_i^{k+1} = Z_i^k + V_i^{k+1} \end{cases} \tag{13}$$

where k represents the iteration number. ω, c_1, and c_2 are the inertia weight coefficient and learning factors, respectively. And r_1 and r_2 represent a random number between 0 and 1.

III. PM Temperature Estimation Method Based on MP-PINN

To accurately estimate the real-time temperature of the PM and provide criteria for diagnosing ID faults in PMSMs, this section proposes a temperature estimation method for PM based on MP-PINN. This method utilizes the dataset obtained from the proposed LPTN, combined with experimentally collected data, to train the neural network, achieving high estimation accuracy and generalization performance.

A. Proposed LPTN of PMSMs

Drawing on the principles of heat transfer theory, LPTNs are specifically formulated to approximate the temperatures of distinct spatially isolated components within a system by modeling the flow of heat through an equivalent circuit diagram. The parameters in this network represent the relevant thermal characteristics of the system's components. The most common structure for an LPTN is typically derived from the heat diffusion equation.

A typical thermal element consists of a thermal capacitance, a power loss source, and multiple thermal resistances leading to other thermal elements. It is also considered a basic block in the LPTN system. The ith thermal element in a LPTN describes:

$$C_i(t)\frac{\mathrm{d}T_i(t)}{\mathrm{d}t} = P_i(t) + \sum_{j \in M} \frac{T_j(t) - T_i(t)}{R_{i,j}(t)} \tag{14}$$

where C_i denotes the thermal capacitance, P_i is the heat source. $R_{i,j}$ is the bidirectional thermal resistance between the temperatures at i and j with $M = \{1, \ldots, i\text{-}1, i{+}1, \ldots, m\}$. T_i and T_j are the actual temperature at i and j.

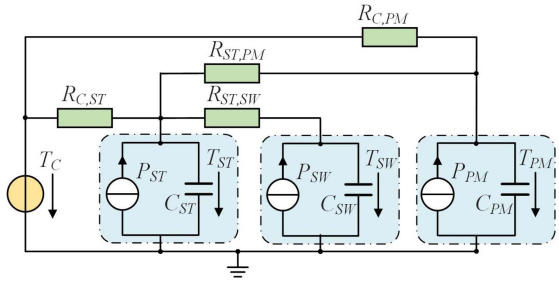

Fig. 1. Low-order LPTN structure for PMSMs.

In this article, a light gray-box LPTN for a PMSM with 3 nodes (the stator tooth, the stator winding, and the PM) and 2 equivalent thermal sources (the ambient and coolant temperature) is built. In Fig. 1, only the dominant heat transfer pathways are taken into account in the low-order physics-based thermal network model, so other heat pathways are thought to be negligible. To describe the low-order LPTN for PMSMs, the following assumptions are made.

1) The temperature distribution within each motor component is assumed to be homogeneous.
2) The temperature of the PM is deemed to be indicative of the temperature of the entire rotor.
3) The temperature of the end-winding is assumed to be equivalent to that of the stator winding in the slot.
4) The heat generation and thermal capacity are uniformly distributed throughout each motor components.
5) The motor power loss is approximately equal to the heat source.

To sum up, the low-order LPTN model can be described as:

$$\begin{aligned} C_{\mathrm{ST}}\frac{dT_{\mathrm{ST}}}{dt} &= P_{\mathrm{ST}} - \frac{T_C - T_{\mathrm{ST}}}{R_{C,\mathrm{ST}}} + \frac{T_{\mathrm{ST}} - T_{\mathrm{SW}}}{R_{\mathrm{ST,SW}}} + \frac{T_{\mathrm{ST}} - T_{\mathrm{PM}}}{R_{\mathrm{ST,PM}}} \\ C_{\mathrm{SW}}\frac{dT_{\mathrm{SW}}}{dt} &= P_{\mathrm{SW}} - \frac{T_{\mathrm{ST}} - T_{\mathrm{SW}}}{R_{\mathrm{ST,SW}}} \\ C_{\mathrm{PM}}\frac{dT_{\mathrm{PM}}}{dt} &= P_{\mathrm{PM}} - \frac{T_{\mathrm{ST}} - T_{\mathrm{PM}}}{R_{\mathrm{ST,PM}}} + \frac{T_C - T_{\mathrm{PM}}}{R_{C,\mathrm{PM}}} \end{aligned} \tag{15}$$

where C_{ST}, C_{SW}, and C_{PM} are the stator tooth, the stator winding, and the PM thermal capacitance, respectively. P_{ST}, P_{SW}, and P_{PM} are the stator tooth, the stator winding, and the PM power loss, respectively. T_{ST}, T_{SW}, and T_{PM} are the stator tooth, the stator winding and the PM temperature, respectively. $R_{\mathrm{ST,SW}}$, $R_{C,\mathrm{PM}}$, $R_{C,\mathrm{ST}}$, and $R_{\mathrm{ST,PM}}$ are the bidirectional thermal resistance between the temperature at the stator tooth and the stator winding, the ambient and the PM, the ambient and the stator tooth, the stator tooth, and the PM, respectively.

According to [35], thermal modeling based on the low-order LPTN method requires consideration of various thermal network parameters.

First, it is necessary to calculate the losses in each part of the PMSM, including P_{ST}, P_{SW}, and P_{PM}. The copper loss P_{Cu} can be calculated in real-time using the motor current, assuming that the copper loss is equal to the stator winding loss P_{SW}:

$$P_{Cu} = 1.5 i_s^2 R_s \tag{16}$$

where i_s is the total motor current, $i_s = \sqrt{i_d^2 + i_q^2}$.

Due to the difficulty of quantitative analysis such as stray loss, it is assumed in this study that the P_{ST} is equal to the stator iron loss P_{irons}, and the P_{PM} is equal to the rotor iron loss P_{ironr}.

The alternating magnetic field generated by the PMSM will induce hysteresis loss and eddy current loss on the stator. Because the magnetic field density in the stator core is not uniform and there are many nonlinear factors such as magnetic saturation, it is difficult to calculate the iron loss accurately in real time. According to the stator iron loss model proposed by Bertotti, the P_{irons} can be divided into three parts: 1) hysteresis loss P_{hys}, 2) eddy current loss P_{edd}, and 3) additional loss P_{ext}:

$$P_{irons} = P_{hys} + P_{edd} + P_{ext}. \tag{17}$$

Through the analysis of different types of losses, the following expression can be obtained:

$$\begin{cases} P_{hys} = k_{hys} f B^2 \\ P_{edd} = k_{edd} (fB)^2 \\ P_{ext} = k_{ext} (fB)^{3/2} \end{cases} \tag{18}$$

where k_{hys}, k_{edd}, and k_{ext} are, respectively, hysteresis loss coefficient, eddy current loss coefficient, and additional loss coefficient, f is motor frequency and B is motor magnetic density.

Due to the influence of the stator slots, the magnetic field in the air gap of the motor is not uniform. Additionally, the switching cycle of the inverter and the nonfundamental components of the winding current introduce magnetic field harmonics to the rotor. Meanwhile, given that the permanent magnet is a large conductor close to the rotor surface, and the rotor is formed by laminating silicon steel sheets, it is reasonable to approximate that the rotor losses are mainly concentrated as eddy current losses in the permanent magnet. The mathematical expression for this is as follows:

$$P_{\mathrm{PM}} = k_{\mathrm{pm}} (fB)^2 \tag{19}$$

where k_{pm} is the eddy current loss coefficient of permanent magnet.

Second, the specific calculation of each heat capacity in low-order LPTN is considered. The C_{SW} can be approximated as:

$$C_{\mathrm{SW}} = \rho_{cu} c_{cu} V_w = N_s N_c \times \pi r_{\mathrm{sw}}^2 \times \rho_{cu} c_{cu} \tag{20}$$

where V_w is the conductor volume, c_{cu} is the specific heat capacity of the conductor, r_{sw} is the radius of the conductor, ρ_{cu} is the density of the conductor, N_s is the number of stator slots of the motor, and N_c is the number of conductors per slot of the motor.

Assuming that the motor stator can be approximated as a silicon steel block with a hollow cylinder minus the slot volume, the C_{SY} can be approximated as:

$$C_{\mathrm{ST}} = \left[\pi \times (R_{\mathrm{rotor}}^2 - R_{\mathrm{shaft}}^2) - \frac{V_w}{\tau} \right] \times c_{ss} \tag{21}$$

where τ is the slot filling rate of the stator winding, and c_{ss} is the specific heat capacity of the silicon steel. Due to the close contact between the PM and the rotor magnetic steel, the PM and the rotor can be regarded as a whole in the thermal network, and the C_{PM} can be calculated in the same way.

Finally, the thermal resistance of the PMSM can be directly calculated based on the motor's geometric dimensions and the physical properties of the materials. This article obtains the thermal resistance through the establishment of finite element simulation of the motor and empirical knowledge.

Thus, it can be seen that the low-order LPTN is a simplified method to simulate the thermal behavior of the PMSM, which estimates the temperature distribution by dividing the motor into several thermal nodes and assuming the heat conduction between these nodes to be linear. Although this method can provide reasonable predictions in some cases, it faces the following issues: oversimplification and difficulty in parameter tuning. Since the LPTN is usually built upon simplified assumptions, such as ignoring the complexity and nonlinear heat transfer mechanisms within the motor, this may lead to inadequate prediction accuracy. Moreover, this method relies on the accurate determination of thermal resistances and capacitances between thermal nodes in the thermal network model, which often requires complex simulations or experimental determinations. For different operating conditions, these parameters might also change, reducing the accuracy of the estimated temperatures of PMSMs.

B. Physics Informed Neural Network

PINN is a type of machine learning approach that combines the power of neural networks with the knowledge of physics. Unlike traditional neural networks, which require massive amounts of labeled data, PINN can learn from limited data while still ensuring the conservation of fundamental physical laws. This is achieved by incorporating the governing equations of a physical system into the neural network architecture.

In the context of motor temperature estimation, PINN can be used to accurately predict the temperature of the motor based on limited experimental data. This is especially important in high-performance applications, where motor temperature can have a significant impact on performance and reliability. By leveraging the physical knowledge of heat transfer and fluid dynamics, PINNs can provide more accurate and reliable temperature estimates than traditional machine learning approaches.

One of the primary components of the PINN is a fully connected NN (FCNN). Each neuron in the network is connected to every neuron in the adjacent layers, forming a fully connected graph structure. The basic principle of FCNN is to use the input data to compute a sequence of nonlinear transformations, leading to a final output. The mathematical equations of a single hidden layer FCNN can be represented as follows:

$$\begin{aligned} I_j &= \sum w_{ji} \cdot x_i + b_j, \\ y_j &= \sigma_h(I_j) \\ I_o &= \sum w_{oj} \cdot y_j + b_o \\ y_o &= \sigma_p(I_o) \\ i &= 1, 2, 3 \ldots, m, j = 1, 2, 3 \ldots, h, o = 1, 2, 3 \ldots, p \end{aligned} \tag{22}$$

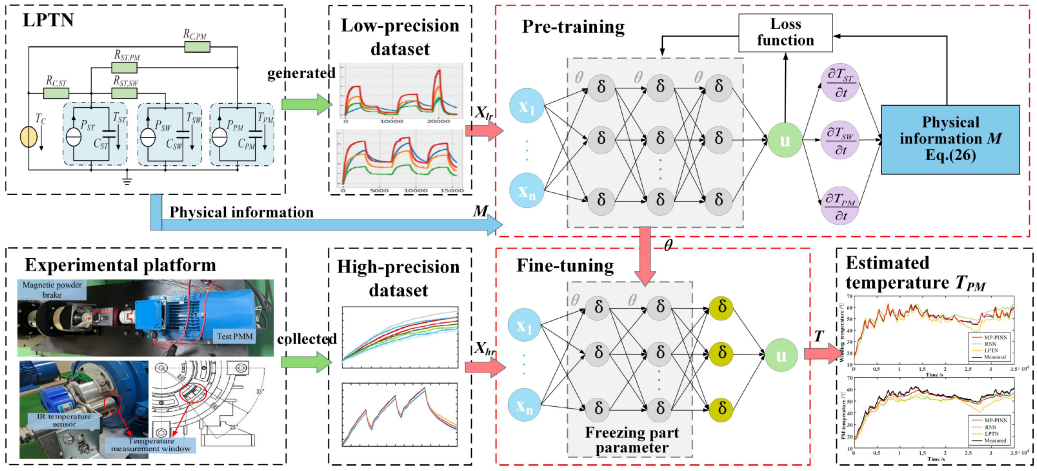

Fig. 2. Schematic representation of the proposed MP-PINN.

where the input layer, the hidden layer, and the output layer have m neurons, h neurons, and p neurons, respectively. w_{ji} and w_{oj} represent the connection weights of the input and hidden layers, the hidden and output layers, respectively; x_i, I_j, and I_o represent the input value of the input layer, the hidden and output layers, respectively; b_j and b_o are the threshold values of the hidden and output layers, respectively; σ_h and σ_p are the activation functions of the hidden and output layers, respectively.

For using the NN in practice, the model parameters need to be estimated. In a data-driven setting, this is achieved by minimizing a loss function. The loss function is used:

$$\text{Loss}_{\text{MSE}} = \frac{1}{k}\sum_{i=1}^{k}(y_i - \hat{y}_i)^2 \tag{23}$$

where y_i denotes the ith output and $\hat{y}_i$is the NN predicted output.

To achieve the goal of integrating data and physical laws, PINN based on the normal loss function is designed a new loss function consisting of physics information. The mathematical formulation of the loss function Loss_A in a PINN can be expressed as follows:

$$\begin{aligned} \text{Loss}_A &= \text{Loss}_{\text{MSE}} + \lambda\text{Loss}_P + \mu\text{Loss}_0 \\ \text{Loss}_P &= \frac{1}{k}\sum_{i=1}^{k}(M)^2 \\ \text{Loss}_0 &= (M_0 - y_0)^2 \end{aligned} \tag{24}$$

where λ and μ are the normalized coefficients. Loss_P is the loss term related to the physics law and Loss_0 is the loss term estimated at the initial condition. M is the physical law equation and M_0 is the physical law equation at $t = 0$.

C. Multiprecision Physics-Informed Neural Network

The motor thermal data-collection is expensive and time-consuming in the laboratory and the temperature sensor is difficult to install inside the motors. So special test motors need to be customized. On the other hand, PMSMs usually work in harsh environments and complex working conditions (such as electric vehicles driving in cities), and this challenging scenario makes the internal temperature distribution of the motor more complex.

To better utilize the known physical laws and the limited experimental data, this article proposes a transfer learning method based on the MP-PINN. The framework proposed is particularly suitable when the physics of the problem is known in an approximate sense and a large amount of simulation data (low-precision data X_l generated by the proposed LPTN) but only a few data for the test motor (high-precision data X_h) are available.

The core idea behind this method is to pretrain the MP-PINN model on low-precision data, which helps to initialize the model's parameters more effectively and reduce its dependence on large datasets. This pretraining step significantly improves the precision of temperature estimation when applied to high-precision data by leveraging the physical knowledge embedded in the low-precision data, thus enhancing the model's ability to generalize from limited experimental data.

A diagram of the MP-PINN process is provided in Fig. 2, and an extensive explanation for each phase within the MP-PINN framework is provided below.

1) *Data Preprocessing*: When gathering low-precision information $X_l \in R^{T_l \times S}$at T_l moments and high-precision $X_h \in R^{T_h \times S}$readings at T_h moments from S sensors (like current, voltage, and temperature detectors), it is crucial to first standardize the data, remove any anomalous readings, and populate any missing entries. At a specific moment t, the recorded data x encompasses merely S variables from sensors, intentionally overlooking any temporal linkages with previous instances $t-1$, $t-2$, and so on.
2) *Feature Extraction*: The preprocessed dataset X_{lp} and X_{hp} may still encompass considerable redundant information. High correlation among the data collected from certain sensors can impede the effective construction of the NN. To address this, feature extraction is imperative. Correlation analysis is commonly employed for feature selection to identify and eliminate variables with high interdependencies. Subsequently, this process results in the refined datasets X_{lr} and X_{hr}.
3) *Pretraining on the Low-Precision Data*: The data X_{lr} is divided into a training dataset X_{ltrain}, a validation dataset X_{lval}, and the target dataset Y_{ltrain}, Y_{lval}. The training and validation datasets are concurrently fed into the fully

Algorithm 1: Transfer Learning With Physics-inform Neural Network.

Input:

Low-precision dataset X_l, high-precision dataset X_h, the proposed low-order LPTN covering motor thermal behavior (3).

Output:

Temperature estimation of PM T_{est}.

1 Preprocessing the original dataset X_l and X_h including data normalization, removing outliers, filling missing values, etc., to obtain the preprocessed dataset X_{lp} and X_{hp}.
2 The feature extraction is performed on the dataset X_{lp} and X_{hp}, the correlation between each variable is calculated, and the variable with strong correlation is eliminated to obtain the dataset X_{lr} and X_{hr}.
3 Train the PINN model on the dataset X_{lr} to encode the proposed low-order LPTN to establish initial NN parameters θ.
4 Integrate obtained from targeted experiments to refine the low-precision PINN model. Employing transfer learning by the high-precision dataset X_{hr} to adjust only the last two layers parameters $\theta^{'}$ of the NN to get the final high-precision model.
5 Obtaining the optimal value and save the corresponding model.
6 Loading the model and input X_{htest} to get the estimation results T_{est} .

connected NN model. The PINN's architecture ensures adherence to physical principles. This involves forward propagation through the intermediate layers, culminating in the output layer where the predictive results are obtained. The formula is as follows:

$$Z = \text{softmax}\left(\sigma\left(\sum \text{w} \cdot \text{x} + \text{b}\right)\right) \tag{25}$$

where softmax is the activation function and b is the bias. During the training phase, the loss function for the low-precision dataset is determined based on:

$$M = \begin{bmatrix} P_{\text{ST}} - \frac{T_C - T_{\text{ST}}}{R_{C,\text{ST}}} + \frac{T_{\text{ST}} - T_{\text{SW}}}{R_{\text{ST,SW}}} + \frac{T_{\text{ST}} - T_{\text{PM}}}{R_{\text{ST,PM}}} - C_{\text{ST}}\frac{dT_{\text{ST}}}{dt} \\ P_{\text{SW}} - \frac{T_{\text{ST}} - T_{\text{SW}}}{R_{\text{ST,SW}}} - C_{\text{SW}}\frac{dT_{\text{SW}}}{dt} \\ P_{\text{PM}} - \frac{T_{\text{ST}} - T_{\text{PM}}}{R_{\text{ST,PM}}} + \frac{T_C - T_{\text{PM}}}{R_{C,\text{PM}}} - C_{\text{PM}}\frac{dT_{\text{PM}}}{dt} \end{bmatrix} = 0. \tag{26}$$

The model parameters θ are iteratively adjusted through training, minimizing the difference between the predicted outputs and the actual sensor data in Y_{ltrain}.

4) *Fine-Tuning on High-Precision Data*: The above process establishes a robust initial parameter set θ for the subsequent high-precision modeling. The data X_{hr} is divided into a training dataset X_{htrain}, a validation dataset X_{hval}, a test dataset X_{htest}, and the target dataset Y_{htrain}, Y_{hval}. Using this dataset to train the last two layers' parameters of the low-precision PINN and to obtain the whole parameters $\theta^{'}$ for the high-precision PINN.

5) *Loading the model and input X_{htest} to get the diagnosis result T_{est}:*

By pretraining on low-precision data, the MP-PINN model is better able to learn the underlying physical principles governing the temperature distribution within the PMSM. This process allows the model to begin with a more accurate set of parameters before being fine-tuned with the high-precision data. Consequently, the model's sensitivity to variations in high-precision data is improved, enabling it to make more accurate predictions even when only limited high-precision data is available.

IV. Temperature-Insensitive ID Fault Diagnosis Based on Dual-State Flux Estimation

Given the variability of PM temperatures, direct fault diagnosis based on flux estimation of irreversible demagnetization faults in motors is challenging. Therefore, this section proposes an ID fault diagnosis based on dual-state ESOs for PMSMs considering temperature influence.

In [36], taking Neodymium magnet (NdFeB), the most commonly used PM material in PMSMs, as an example, the B-H curves at different temperatures demonstrate the changes in the magnetic hysteresis loops of the material from 23 °C to 180 °C. As the temperature increases, the hysteresis loops gradually shift from the left to the right side, indicating a decrease in magnetic induction for the same magnetic field strength, which signifies a reduction in magnetic performance with rising temperature. Additionally, the knee point of the hysteresis loop, where rapid demagnetization of the magnet begins, shifts to the right with increasing temperature. Typically, the operating point of a motor is designed to the right of the knee point to avoid rapid demagnetization.

In order to further quantitatively analyze the influence of temperature on the magnetism of PM, the residual magnetism of NdFeB is studied separately. With the increase in temperature, the residual magnetic induction intensity gradually decreases, showing a nearly linear negative correlation. Equation (27) represents the relationship between the residual magnetic ratio ψ_{thr} and temperature T_{PM}:

$$\Psi_{thr} = B_r(T_{\text{PM}})/B_{r0}(23^{\circ}C) = k_T T_{\text{PM}} + k_0 \tag{27}$$

where $B_r(T_{\text{pm}})$ is the remanence of the PM under T_{pm}, B_{r0}(23 °C) is the remanence of the PM under 23 °C, and k_T and k_0 are temperature-related parameters.

After obtaining accurate motor flux linkage and permanent magnet temperature, it can be used to determine whether ID fault has occurred. As shown in Fig. 3, specifically, if the error ratio err_f between ψ_{f_cal} and initial flux is smaller than the residual magnetic ratio ψ_{thr}, ID fault occurs in the PMSM. Otherwise, the PMSM is healthy. The diagnosis equation for irreversible demagnetization fault can be written as:

$$\begin{cases} err\_f = \Psi_{f\_cal}/\Psi_f \\ err\_f \geq \Psi_{thr}, \ \text{health} \\ err\_f < \Psi_{thr}, \ \text{ID fault occurs.} \end{cases} \tag{28}$$

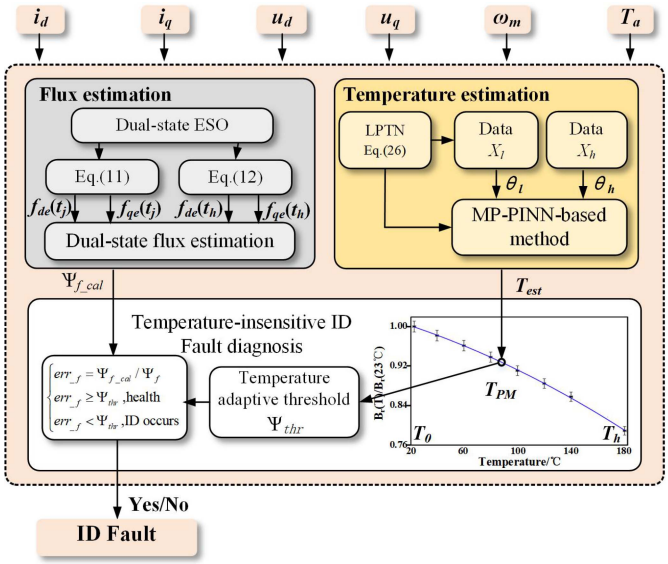

Fig. 3. Topology of the proposed temperature-insensitive ID fault diagnosis method based on dual-state flux estimation.

TABLE I
MOTOR PROTOTYPE PARAMETERS

Parameter	VALUE	Unit
Number of pole pairs p	2	-
d-axis inductance L_d	28.2	mH
q-axis inductance L_q	62.63	mH
Phase resistance R_s	1.469	Ω
Magnet flux Ψ_f	0.636	Wb
Moment of inertia J	0.003	kg/m^2
Rated speed n	600	rpm
Rated load T_l	4	N·m

The Ψ_{thr} is accurately determined through experimental calibration by correlating magnetic behavior at different operating temperatures with performance degradation, as described in (27).

V. VERIFICATIONS

To verify the proposed ID fault diagnosis method, experiments are conducted on the 24-slot/4-pole interior PMSMs. And the parameters of the healthy test motor are given in Table I. Besides, to simulate the condition of PM demagnetization, one motor is specially customized. In one motor, all PMs are magnetized to 90% of their rated value, representing a 10% demagnetization fault. It is important to note that while the experimental validation in this article uses a motor with 90% magnetization, the proposed method is not limited to this specific case and can be applied to other magnetization levels. The selection of 90% magnetization is based on practical engineering relevance and experimental feasibility. In industrial applications, 10% irreversible demagnetization is commonly used as a fault diagnosis threshold, and at this level, key motor performance parameters begin to attenuate while the motor remains operational, making it an ideal condition for evaluating the proposed detection method. The experimental setup is shown in Fig. 4.

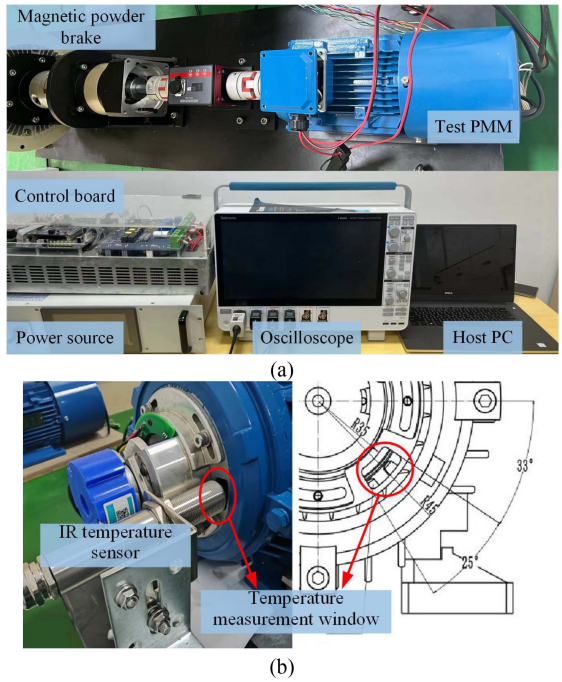

Fig. 4. Test bench used for verification.

Regarding the hardware setup, algorithms for testing were run on a DSP TMS320F 28335 controller board. Monitoring of data occurs through a control console on the primary PC, with an oscilloscope capturing the data. To provide necessary load, a magnetic powder brake is linked to the motor under test.

In order to achieve real-time detection of the temperature of the coil and stator tooth temperature of the health PMSM, the platform uses PT100 temperature sensors to obtain accurate temperature data. A number of PT100 sensors are evenly distributed at different locations within the test motor to fully monitor the temperature distribution of the motor during operation. It is worth mentioning that, to measure the temperature of the motor rotor, as shown in Fig. 4(b), a measurement window was created on the motor's rear cover for rotor temperature measurement. And an infrared sensor is positioned to measure the rotor's real-time temperature without making direct contact.

A. Validation of the Dual-State ESO-Based Flux Estimation Method

In order to prove the effectiveness of the motor flux estimation method based on ESO, experiments were carried out on the motor platform. The setup of this experiment is as follows: two motors (a healthy motor and a faulty motor with uniform demagnetization of 10%) are tested, respectively, to identify the flux value of the motors under different working conditions (including speed, torque, and PM temperature). The working condition design of the two test motors is shown in Table II.

In Figs. 5 and 6, the operational performance of the healthy PMSM under case 1, along with the parameter estimates derived from both the proposed method and a traditional sliding mode flux observer (SMFO). Primarily, it is evident that the motor

TABLE II
WORKING CONDITION DESIGN OF THE TEST PMSMS

Case	Speed/rpm	Torque/N·m	Notes
1	600	4	
2	600	2	Motor is started, with the
3	400	4	temperature T_A.
4	400	2	
5	600	4	Motor has been running for 4
6	400	2	hours, with unknown temperature.
7	600	4	Motor has been running for 2
8	400	2	hours, with unknown temperature.

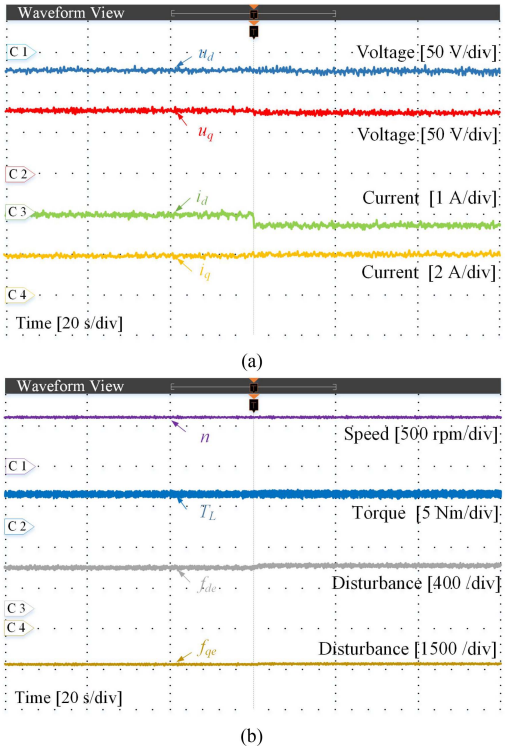

Fig. 5. Performance of the healthy PMSM under case 1. (a) Motor current and voltage. (b) Motor torque and disturbance.

currents closely follow their reference values. As intended, there is a jump in the i_d from -0.1 A to -0.25 A at 60 s, while i_q remains stable at approximately 2.1 A. Moreover, the voltages on the dq-axis exhibit minimal variation, and the observed disturbance values on the dq-axis swiftly stabilize following changes in current. Subsequently, under steady conditions in case 1, the proposed method yields estimates for L_{d_cal}, L_{q_cal}, R_{s_cal}, and Ψ_{f_cal} at 28.9 mH, 62.6 mH, 1.46 Ω, and 0.64 Wb, respectively, aligning closely with their actual values and, thus, validating the algorithm's efficacy. Finally, when the motor reaches a stable speed of 600 rpm under 4 N·m, the estimated flux value Ψ^*_f, as observed by the SMFO, is 0.64 Wb, matching the true value. This indicates that the traditional method is effective at room temperature without parameter mismatches in a healthy motor.

The proposed SMFO method is used to identify the parameters of the healthy PMSM under 8 different conditions, as shown in Table III. It can be observed that due to variations in operating conditions, slight differences in motor parameter identification

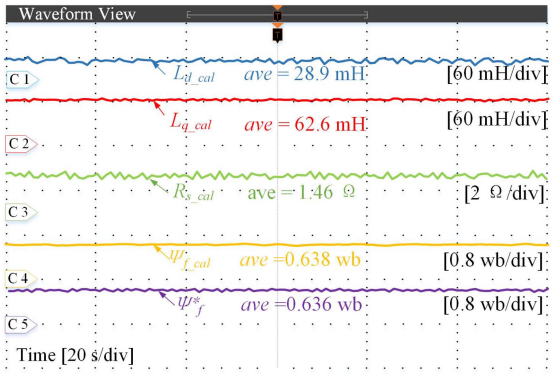

Fig. 6. Parameter identification results of the healthy PMSM under case 1.

TABLE III
ESTIMATED PARAMETERS OF THE HEALTHY MOTOR UNDER DIFFERENT WORKING CONDITIONS

Case	L_{d_cal} (mH)	L_{q_cal} (mH)	R_{s_cal} (Ω)	Ψ_{f_cal} (Wb)	Ψ^*_f (Wb)
1	28.9	62.6	1.46	0.638	0.636
2	30.2	64.3	1.46	0.625	0.630
3	28.8	62.2	1.47	0.641	0.640
4	30.1	64.0	1.46	0.636	0.631
5	26.9	59.0	1.79	0.608	0.623
6	28.2	60.7	1.77	0.605	0.587
7	27.2	60.2	1.56	0.621	0.626
8	28.5	61.8	1.54	0.627	0.591

results occur, which can be attributed to the presence of armature reaction and the impact of motor structure, as extensively studied in [37]. With an increase in load, there is a slight increase in the motor's dq-axis inductance. Furthermore, a comparison of case 1, 5, and 7 reveals that with an increase in internal motor temperature, the dq-axis inductance and flux linkage decrease, while the resistance value increases. Comparing the flux linkage values estimated by both algorithms shows that at room temperature and under a rated load of 4 N·m, the SMFO's values are close to the actual values, indicating high precision. However, as temperature rises and conditions change, causing other parameters to change, the precision of the traditional method decreases. This demonstrates the superiority of the proposed method, which can accurately identify flux linkage without being affected by changes in operating conditions and parameters.

Figs. 7 and 8 illustrate the performance of a faulty PMSM operating under case 1 and the parameter estimates ascertained by the proposed and traditional method. Initially, similar to the healthy motor operation, the current tracks the reference values well, with a designed step from -0.1 A to -0.25 A on i_d at 60 s. However, due to the demagnetization fault, i_q stabilizes at 2.3 A, and the dq-axis voltages remain essentially unchanged, with observed dq-axis disturbances quickly settling after the current shift. Subsequently, when the motor stabilizes under condition 1, the estimated results for the d-axis inductance, q-axis inductance, resistance, and flux linkage by the proposed method are 34.9 mH, 58.5 mH, 1.46 Ω, and 0.579 Wb, respectively, which are close to the actual values for a motor with 10% uniform demagnetization, substantiating the effectiveness

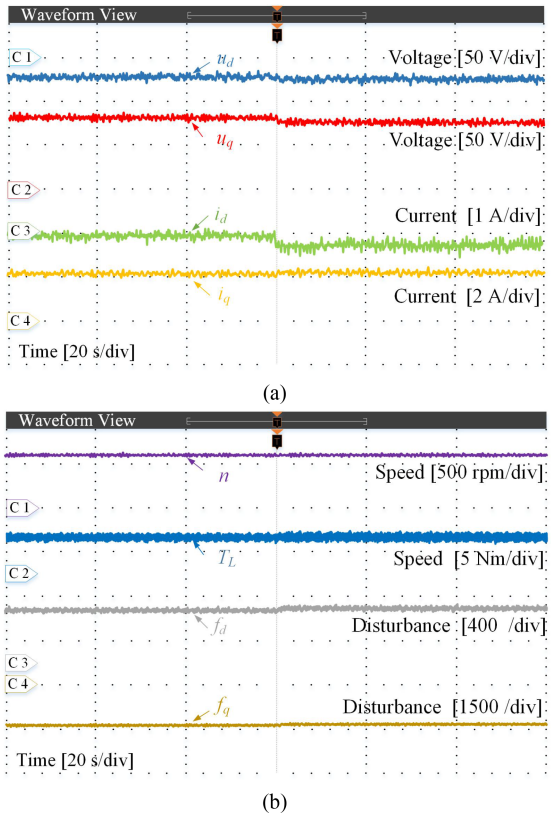

Fig. 7. Performance of the faulty PMSM under case 1. (a) Motor current and voltage. (b) Motor torque and disturbance.

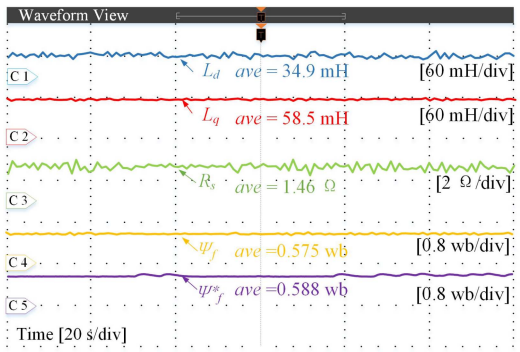

Fig. 8. Parameter identification results of the faulty PMSM under case 1.

of the method. Thirdly, at 600 rpm with 4 N·m, the SMFO estimates the flux linkage to be 0.588 Wb. Due to changes in the magnetic properties, this estimated inductance differs from the known healthy motor values. However, during testing, the induction inductance of the healthy motor was still used to construct the observer, leading to a flux linkage estimation slightly above the real value. This underscores the proposed method's ability to detect flux linkages more accurately than the traditional approach.

The proposed SMFO is employed to identify the parameters of the faulty PMSM under 8 different operating conditions, as displayed in Table IV. The results show that as the load increases, there is a slight rise in the *dq*-axis inductance of the motor.

TABLE IV
ESTIMATED PARAMETERS OF THE FAULTY MOTOR UNDER DIFFERENT WORKING CONDITIONS

Case	L_{d_cal} (mH)	L_{q_cal} (mH)	R_{s_cal} (Ω)	Ψ_{f_cal} (Wb)	Ψ^*_f (Wb)
1	34.9	58.5	1.46	0.575	0.588
2	39.5	61.4	1.47	0.561	0.555
3	31.8	58.2	1.47	0.579	0.608
4	37.5	60.3	1.46	0.568	0.565
5	32.0	56.3	1.73	0.545	0.578
6	37.8	57.1	1.75	0.552	0.542
7	32.7	56.9	1.55	0.562	0.530
8	37.0	57.8	1.58	0.558	0.510

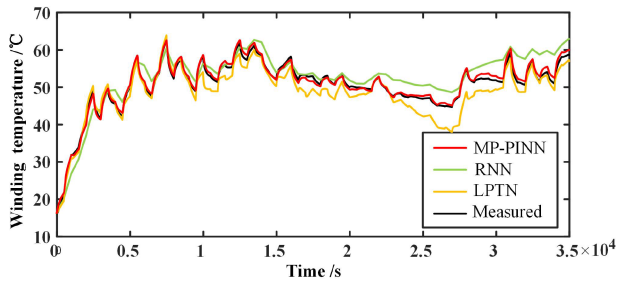

Fig. 9. Winding temperature estimated by different methods.

Further analysis of case 1, 5, and 7 reveals that with an elevation in the motor's internal temperature, both the *dq*-axis inductance and flux linkage decrease, whereas the resistance value shows an opposite trend. Comparing the flux linkage values estimated by both algorithms, it is evident that at room temperature with 4 N·m, the SMFO closely matches the real values, showcasing high precision. However, with changing temperature conditions that lead to other parameter alterations, the accuracy of the traditional method declines. This highlights the advantage of the proposed algorithm, which, unaffected by variations in operating conditions or parameters, can accurately discern the values of flux linkage.

B. Validation of the PM Temperature Estimation Method Based on MP-PINN

At the initial stage of the method, according to the low-order thermal network model established previously, the data required by the neural network is generated (low-precision data), which aims to meet the basic needs of neural network training. Through this low-precision data, the MP-PINN model can be pretrained, and on this basis, its network parameters are established. Then, the parameters of the pretrained model are fine-tuned by using the high-precision data set collected by the temperature measurement platform of the permanent magnet traction motor, and a perfect MP-PINN model is constructed, which could accurately predict the temperature of the motor. Meanwhile, to minimize the computational load on the embedded system while ensuring real-time monitoring of the PM temperature, we set the estimation interval to 1 s.

As observed from Fig. 9 and Table V, the accuracy of motor winding temperature estimation improves progressively from thermal network-based methods (LPTN) to data-driven

TABLE V
PERFORMANCE INDEXES OF WINDING TEMPERATURE ESTIMATION BY DIFFERENT METHODS

Method	MAE (°C)	RMSE (°C)	MAPE	R^2
MP-PINN	0.718	0.829	1.406%	0.986
RNN	2.651	3.186	5.283%	0.796
LPTN	2.679	3.211	5.196%	0.793
GRU	2.723	3.234	5.369%	0.790
LSTM	2.733	3.244	5.388%	0.788
PINN	1.945	2.317	3.952%	0.892
MPNN	2.232	2.602	4.460%	0.864

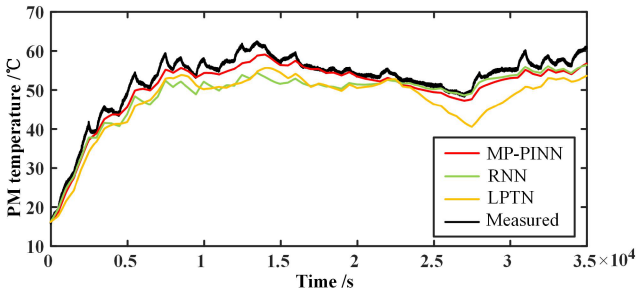

Fig. 10. PM temperature estimated by different methods.

TABLE VI
PERFORMANCE INDEXES OF PM TEMPERATURE ESTIMATION BY DIFFERENT METHODS

Method	MAE (°C)	RMSE (°C)	MAPE	R^2
MP-PINN	1.960	2.250	3.709%	0.927
RNN	3.377	4.015	6.113%	0.766
LPTN	5.099	5.537	9.631%	0.553
GRU	3.890	4.251	7.042%	0.738
LSTM	3.819	4.170	6.945%	0.748
PINN	2.898	3.300	5.286%	0.842
MPNN	3.043	3.763	5.459%	0.795

approaches (recurrent neural network, RNN; gated recurrent unit, GRU; long short-term memory, LSTM) and finally to the proposed MP-PINN algorithm. The MP-PINN algorithm achieves the lowest error metrics, with an MAE of 0.718 °C, RMSE of 0.829 °C, MAPE of 1.406%, and R2 of 0.986, significantly outperforming all other methods. In contrast, traditional LPTN methods show much larger errors (e.g., an MAE of 2.679 °C and RMSE of 3.211°C), while GRU and LSTM methods, despite leveraging advanced time-series processing capabilities, still show inferior performance compared to MP-PINN (e.g., LSTM: MAE of 2.733 °C, RMSE of 3.244 °C, R2 of 0.788). This improvement by MP-PINN is due to the integration of physical laws, enabling accurate estimation even under conditions not covered by the training data.

From Fig. 10 and Table VI, a similar trend is observed in the estimation of PM temperature. The MP-PINN algorithm outperforms all other methods, achieving an MAE of 1.960 °C, RMSE of 2.250 °C, MAPE of 3.709%, and R2 of 0.927. Compared to MP-PINN, GRU, and LSTM exhibit higher errors, with MAEs of 3.890 °C and 3.819 °C, respectively, and lower R2 values (e.g., 0.704 for GRU and 0.718 for LSTM). The estimation accuracy of PM temperature across all methods is generally lower than

TABLE VII
ID FAULT DIAGNOSIS OF THE HEALTHY PMSM UNDER DIFFERENT WORKING CONDITIONS

Case	T_{est} (°C)	T_{pm} (°C)	Ψ_{thr}	Ψ_{f_cal} (Wb)	Ψ^*_f (Wb)	err_f	ID Fault
1	17.8	17.8	/	0.638	0.638	/	No
2	17.9	17.9	/	0.625	0.625	/	No
3	18.1	18.1	/	0.641	0.641	/	No
4	18.0	18.0	/	0.636	0.636	/	No
5	78.2	78.9	94.0%	0.608	0.638	95.3%	No
6	78.2	79.3	94.0%	0.605	0.636	95.1%	No
7	52.4	53.6	96.7%	0.621	0.638	97.3%	No
8	53.3	54.6	96.6%	0.627	0.636	98.5%	No

for winding temperature. This is because the PM is affected by the complex environment and multiple losses inside the motor rotor, and the temperature change has a more complex law. On the other hand, the temperature of the PM is measured by the infrared noncontact temperature sensor, and the rotor is a rotating object. So, the measurement of the temperature of the PM has a greater error than the measurement of the winding temperature. However, MP-PINN still achieves superior accuracy, demonstrating its ability to account for complex thermal behavior.

The results of the ablation study from Tables V and VI further validate the effectiveness of MP-PINN. The multiprecision neural network (MPNN), which excludes physical information, achieves an MAE of 2.232 °C and RMSE of 2.602 °C in winding temperature estimation, while the PINN model, which excludes multiprecision data, performs slightly better but still falls short with an MAE of 1.945 °C and RMSE of 2.302 °C. In PM temperature estimation, the MPNN and PINN models show similarly inferior performance, with RMSEs of 3.763 °C and 3.300 °C, respectively, compared to 2.250 °C for MP-PINN. These results highlight the importance of integrating both physical information and multiprecision data into the framework, as each component contributes significantly to improving the model's accuracy and robustness.

In conclusion, the proposed MP-PINN algorithm achieves significantly better performance in both winding and PM temperature estimation compared to LPTN, RNN, GRU, and LSTM, as well as the ablated versions of the model. The integration of physical laws and multiprecision data is crucial to its success, enabling it to deliver robust and accurate predictions even under complex operating conditions. These results confirm the effectiveness and reliability of MP-PINN for real-world applications in motor temperature monitoring and fault diagnosis.

C. Validation of the Temperature-Insensitive ID Diagnosis in PMSM Based on Dual-State Flux Estimation

Building upon the methods described above, this article proposes a real-time estimation algorithm for rotor temperature based on a multiprecision physical information neural network. Temperature monitoring and analysis of both normally operating motors and motors with faults are conducted under various operating conditions. Additionally, the motor flux linkage values are obtained using an ESO-based flux linkage estimation method. The relevant data are detailed in Tables VII and VIII.

TABLE VIII
ID FAULT DIAGNOSIS OF THE FAULTY PMSM UNDER DIFFERENT WORKING CONDITIONS

Case	T_{est} (°C)	T_{pm} (°C)	Ψ_{thr}	Ψ_{f_cal} (Wb)	Ψ^*_f (Wb)	err_f	ID Fault
1	20.1	20.1	/	0.575	0.638	90.1%	Yes
2	19.8	19.8	/	0.561	0.625	89.7%	Yes
3	19.8	19.8	/	0.579	0.641	90.3%	Yes
4	19.9	19.9	/	0.568	0.636	89.3%	Yes
5	81.2	82.9	93.7%	0.545	0.638	85.4%	Yes
6	82.0	83.7	93.6%	0.552	0.636	85.7%	Yes
7	53.7	54.6	96.5%	0.562	0.638	88.1%	Yes
8	54.1	55.4	96.5%	0.558	0.636	87.7%	Yes

Table VII illustrates the results for the healthy PMSM under various operating conditions. The estimated flux linkage values (Ψ_{f_cal}) are compared with the reference flux values (Ψ_f). The error ratio (err_f) is calculated, where the residual magnetic ratio (Ψ_{thr}) is determined based on the motor's temperature. For all healthy PMSMs (Cases 1–8), the error ratio remains above the Ψ_{thr}, indicating that the motor is healthy using (28). This confirms that the flux estimation method is highly accurate, and the motor's magnetic performance remains consistent with expected values despite varying temperatures.

Table VIII presents the results for a PMSM with ID faults. The error ratios for faulty PMSMs (Cases 1–8) consistently fall below the Ψ_{thr}, as shown by the errors ranging from 85.4% (Case 5) to 90.3% (Case 3). These error ratios are much lower than those for the healthy motor, indicating that the motor has experienced irreversible demagnetization of the PMs. This significant deviation confirms the presence of ID faults in the PMSM, as the magnetic performance has degraded beyond the acceptable threshold.

These results confirm that the proposed method provides a reliable and accurate diagnosis for PMSMs. The error ratio in combination with the temperature-dependent threshold flux enables clear differentiation between reversible temperature variations and ID faults, even under varying temperature conditions.

VI. CONCLUSION

This article presents an ID diagnosis method in PMSMs using MP-PINN-based temperature estimation. The main contributions and novelties can be summarized as follows: First, the proposed MP-PINN method enhanced the temperature estimation accuracy by integrating empirical data and physical laws, demonstrating superior performance in predicting real-time PM temperatures. Second, the ESO-based flux estimation approach provided a robust solution for accurately determining magnetic flux in PMSMs under varying operational conditions and demagnetization states. Finally, experimental validation confirmed the effectiveness of the proposed diagnostic strategy, showcasing its potential in detection of ID faults, thereby contributing to the reliable and efficient operation of PMSM-driven systems. The proposed MP-PINN algorithm has room for optimization when applied to different motor types. This is indeed a key area we plan to explore in future research. Meanwhile, the experimental validation will be extended by testing the proposed method on motors with different demagnetization levels to further demonstrate its effectiveness.

REFERENCES

[1] Z. Q. Zhu and Y. Liu, "Analysis of air-gap field modulation and magnetic gearing effect in fractional-slot concentrated-winding permanent-magnet synchronous machines," *IEEE Trans. Ind. Electron.*, vol. 65, no. 5, pp. 3688–3698, May 2018.

[2] C. Gong, Y. Hu, J. Gao, Y. Wang, and L. Yan, "An improved delay-suppressed sliding-mode observer for sensorless vector-controlled PMSM," *IEEE Trans. Ind. Electron.*, vol. 67, no. 7, pp. 5913–5923, Jul. 2020.

[3] E. Gundabattini, A. Mystkowski, A. Idzkowski, and D. G. Solomon, "Thermal mapping of a high-speed electric motor used for traction applications and analysis of various cooling methods—A review," *Energies*, vol. 14, 2021, Art. no. 1472.

[4] J. Gao, W. Gui, C. Yang, T. Peng, J. Luo, and C. Yang, "Demagnetization modeling and analysis for MTPA-driven permanent magnet motors with distributed lap windings," in *Proc. IEEE Appl. Power Electron. Conf. Expo.*, 2023, pp. 1352–1357.

[5] J. Gao et al., "Modeling, analysis, and suppression of demagnetization for MTPA-driven permanent magnet motors with distributed windings," *IEEE Trans. Power Electron.*, vol. 39, no. 8, pp. 9430–9445, Aug. 2024.

[6] G. Feng, C. Lai, and N. C. Kar, "Expectation-maximization particle-filter- and Kalman-filter-based permanent magnet temperature estimation for PMSM condition monitoring using high-frequency signal injection," *IEEE Trans. Ind. Inform.*, vol. 13, no. 3, pp. 1261–1270, Jun. 2017.

[7] S. Yin, X. Li, J. Gao, A. Chen, and Y. Han, "A novel demagnetization fault diagnosis scheme for the IPM motor without parameter estimation," *IEEE Trans. Power Electron.*, vol. 39, no. 12, pp. 15468–15473, Dec. 2024.

[8] J. Faiz and E. Mazaheri-Tehrani, "Demagnetization modeling and fault diagnosing techniques in permanent magnet machines under stationary and nonstationary conditions: An overview," *IEEE Trans. Ind. Appl.*, vol. 53, no. 3, pp. 2772–2785, May/Jun. 2017.

[9] Z. Meiwei, L. Weili, and T. Haoyue, "Demagnetization fault diagnosis of the permanent magnet motor for electric vehicles based on temperature characteristic quantity," *IEEE Trans. Transp. Electrific.*, vol. 9, no. 1, pp. 759–770, Mar. 2023.

[10] K.-W. Lee, J. Hong, S. B. Lee, and S. Lee, "Quality assurance testing for magnetization quality assessment of BLDC motors used in compressors," *IEEE Trans. Ind. Appl.*, vol. 46, no. 6, pp. 2452–2458, Nov./Dec. 2010,.

[11] A. Specht, O. Wallscheid, and J. B'ocker, "Determination of rotor temperature for an interior permanent magnet synchronous machine using a precise flux observer," in *Proc. Int. Power Electron. Conf.*, 2014, pp. 1501–1507.

[12] S. Stipetic, M. Kovacic, Z. Hanic, and M. Vrazic, "Measurement of excitation winding temperature on synchronous generator in rotation using infrared thermography," *IEEE Trans. Ind. Electron.*, vol. 59, no. 5, pp. 2288–2298, May 2012.

[13] C. Mejuto, M. Mueller, M. Shanel, A. Mebarki, M. Reekie, and D. Staton, "Improved synchronous machine thermal modelling," in *Proc. 8th Int. Conf. Elect. Mach.*, 2008, pp. 1–6.

[14] T. Meng and P. Zhang, "A review of thermal monitoring techniques for radial permanent magnet machines," *Machines*, vol. 10, p. 18, 2022.

[15] W. Kirchgässner, O. Wallscheid, and J. Böcker, "Data-driven permanent magnet temperature estimation in synchronous motors with supervised machine learning: A benchmark," *IEEE Trans. Energy Convers.*, vol. 36, pp. 2059–2067, Sep. 2021.

[16] B. Fahimi and A. Khoobroo, "Methods and apparatuses for fault management in permanent magnet synchronous machines using the field reconstruction method," U.S. Patent 8314576 A1, 2012.

[17] J. Lai, C. Zhou, J. Su, M. Xie, J. Liu, and T. Xie, "A permanent magnet flux linkage estimation method based on Luenberger observer for permanent magnet synchronous motor," in *Proc. 22nd Int. Conf. Elect. Mach. Syst.*, 2019, pp. 1–6.

[18] Z. Yin, G. Li, Y. Zhang, J. Liu, X. Sun, and Y. Zhong, "A speed and flux observer of induction motor based on extended Kalman filter and Markov chain," *IEEE Trans. Power Electron.*, vol. 32, no. 9, pp. 7096–7117, Sep. 2017.

[19] S. Chen, Y. Han, Y. Liu, Z. Ma, C. Gong, and G. Lin, "Precise demagnetization fault diagnosis based on multiple robust sliding mode observers for PMSMs under variable conditions," *IEEE J. Emerg. Sel. Topics Power Electron.*, vol. 13, no. 2, pp. 1747–1757, Apr. 2025, doi: 10.1109/JESTPE.2024.3454293.

[20] Y. Han, S. Chen, C. Gong, X. Zhao, F. Zhang, and Y. Li, "Accurate SM disturbance observer-based demagnetization fault diagnosis with parameter mismatch impacts eliminated for IPM motors," *IEEE Trans. Power Electron.*, vol. 38, no. 5, pp. 5706–5710, May 2023.
[21] H. Ryan, H. Thomas, P. Xiaoze, and V. Christopher, "Real-time temperature prediction of electric machines using machine learning with physically informed features," *Energy AI*, vol. 14, 2023, Art. no. 100288.
[22] O. Wallschied, "Thermal monitoring of electric motors: State-of-the-art review and future challenges," *IEEE Open J. Ind. Appl.*, vol. 2, pp. 204–223, 2021.
[23] D. D. Reigosa, D. Fernandez, H. Yoshida, T. Kato, and F. Briz, "Permanent-magnet temperature estimation in PMSMs using pulsating high-frequency current injection," *IEEE Trans. Ind. Appl.*, vol. 51, no. 4, pp. 3159–3168, Jul./Aug. 2015.
[24] J. Feng, D. Liang, Z. Q. Zhu, S. Guo, Y. Li, and A. Zhao, "Improved low-order thermal model for critical temperature estimation of PMSM," *IEEE Trans. Energy Convers.*, vol. 37, no. 1, pp. 413–423, Mar. 2022.
[25] E. Gundabattini and A. Mystkowski, "Review of air-cooling strategies, combinations and thermal analysis (experimental and analytical) of a permanent magnet synchronous motor," *Proc. Inst. Mech. Engineers, C, J. Mech. Eng. Sci.*, vol. 236, pp. 655–668, 2022.
[26] W. Kirchgässner, O. Wallscheid, and J. Böcker, "Estimating electric motor temperatures with deep residual machine learning," *IEEE Trans. Power Electron.*, vol. 36, no. 7, pp. 7480–7488, Jul. 2021.
[27] J. Lee and J.-I. Ha, "Temperature estimation of PMSM using a difference-estimating feedforward neural network," *IEEE Access*, vol. 8, pp. 130855–130865, 2020.
[28] Y. Wang et al., "Multiscale feature fusion and semi-supervised temporal-spatial learning for performance monitoring in the flotation industrial process," *IEEE Trans. Cybern.*, vol. 54, no. 2, pp. 974–987, Feb. 2024.
[29] A. L'Heureux, K. Grolinger, H. F. Elyamany, and M. A. M. Capretz, "Machine learning with big data: Challenges and approaches," *IEEE Access*, vol. 5, pp. 7776–7797, 2017.
[30] L. Lu, X. Meng, Z. Mao, and G. E. Karniadakis, "DeepXDE: A deep learning library for solving differential equations," *SIAM Rev.*, vol. 63, pp. 208–228, 2021.
[31] D. Jagtap, D. M. Ameya, and G. E. Karniadakis, "Deep learning of inverse water waves problems using multi-fidelity data: Application to Serre-Green-Naghdi equations," *Ocean Eng.*, vol. 248, 2022, Art. no. 110775.
[32] O. Wallscheid and J. Böcker, "Design and identification of a lumped-parameter thermal network for permanent magnet synchronous motors based on heat transfer theory and particle swarm optimisation," in *Proc. 17th Eur. Conf. Power Electron. Appl.*, 2015, pp. 1–10.
[33] Z. Gao, "Scaling and bandwidth-parameterization based controller tuning," in *Proc. Amer. Control Conf.*, 2003, pp. 4989–4996.
[34] L. Xu, S. Zhuo, J. Liu, S. Jin, Y. Huangfu, and F. Gao, "Advancement of active disturbance rejection control and its applications in power electronics," *IEEE Trans. Ind. Appl.*, vol. 60, no. 1, pp. 1680–1694, Jan./Feb. 2024.
[35] O. Wallscheid and J. Böcker, "Global identification of a low-order lumped-parameter thermal network for permanent magnet synchronous motors," *IEEE Trans. Energy Convers.*, vol. 31, no. 1, pp. 354–365, Mar. 2016.
[36] W. Gao, X. Kang, J. Zhang, and Z. Chi, "Determining the maximum operating temperature of permanent magnets via in-situ measurement of the magnetic flux," *J. Magnetism Magn. Mater.*, vol. 562, 2022, Art. no. 169744.
[37] X. Liu, H. Chen, J. Zhao, and A. Belahcen, "Research on the performances and parameters of interior PMSM used for electric vehicles," *IEEE Trans. Ind. Electron.*, vol. 63, no. 6, pp. 3533–3545, Jun. 2016.

Jinqiu Gao was born in Shaanxi Province, China, Jan. 7, 1996. She received the B.Eng. and M.Eng. degrees in electrical engineering from Northwestern Polytechnical University, Xi'an, China, in 2017 and 2020, respectively, and the Ph.D. degree in control science and engineering from the School of Automation, Central South University, Changsha, China, in 2024.

She is currently a Lecturer with the School of Water Resources and Hydropower Engineering, Xi'an University of Technology, Xi'an, China. Her research interests include electrical machine drives and motor fault diagnosis.

Weihua Gui (Member, IEEE) received the B.Eng. degree in electrical engineering and the M.Eng. degree in automatic control engineering from Central South University, Changsha, China, in 1976 and 1981, respectively.

From 1986 to 1988, he was a Visiting Scholar with University Duisburg-Essen, Duisburg, Germany. From 1991 to 2018, he was a Full Professor with the School of Automation, Central South University. Since 2019, he has been a Full Professor with the School of Automation, Central South University. Since 2013, he has been an Academician of Chinese Academy of Engineering. His main research interests include the modeling and optimal control of complex industrial processes, fault diagnoses, and distributed robust control.

Xiaotian Xie (Member, IEEE) received the Ph.D. degree in industrial engineering from the University of Illinois at Urbana-Champaign, Urbana, IL, USA, in 2022.

She is currently an Assistant Professor with the School of Automation, Central South University (CSU), Changsha, China. Before that, she was a Postdoctoral Research Fellow with CSU, from 2022 to 2024. Her current research interests include graph neural networks, network inference, fault diagnosis, and system identification.

Rongchun Wan was born in Shandong Province, China. He received the B.Eng. degree in automation engineering in Jun. 30, 2023 from Central South University, Hunan Province, China, where he is currently working toward the Ph.D. degree in automation engineering.

His research interests include motion control, rail transit energy storage, energy-saving optimization, and energy management.

Shicai Yin received the M.Eng. degree in mechanical design and theory from the China University of Mining and Technology, Xuzhou, China, in 2020, and the Ph.D. degree in control science and engineering from Central South University, Changsha, China, in 2024.

From Jan. 2024 to Nov. 2024, he was a Visiting Doctoral Student with the Nanyang Technological University, Singapore. His research interests include fault diagnosis and optimization control for complex systems.

Chunhua Yang (Fellow, IEEE) received the M.Eng. degree in automatic control engineering and the Ph.D. degree in control science and engineering from Central South University, Changsha, China, in 1988 and 2002, respectively.

She was with the Department of Electrical Engineering, Katholieke Universiteit Leuven, Leuven, Belgium, from 1999 to 2001. She is currently a Full Professor with Central South University. Her current research interests include modeling and optimal control of complex industrial processes, intelligent control systems, and fault-tolerant computing of real-time systems.